

# Dynamic layer formation in the reattachment zone for a supersonic laminar separated flow

Proc IMechE Part G:  
J Aerospace Engineering  
0(0) 1–13  
© IMechE 2019  
Article reuse guidelines:  
sagepub.com/journals-permissions  
DOI: 10.1177/0954410018809600  
journals.sagepub.com/home/pig



Valeriy I Zapryagaev , Ivan N Kavun and Lukeriya P Trubitsyna

## Abstract

In this work, results of an experimental study of the flow structure in the region of reattachment of a supersonic laminar separated flow are reported. The separated flow is generated by a model shaped as a compression corner consisting of a horizontal flat plate followed by a ramp. The model width is equal to the plate length from the leading edge to the plate/ramp junction line. The ramp angle is varied in the interval  $\varphi = 20^\circ$ – $50^\circ$ . The free-stream Mach number is  $M_\infty = 6$  or 8. The analysis of the Pitot pressure profiles near the ramp wall in the downstream direction behind the reattachment line confirms the existence of a high-pressure layer with the total pressure being appreciably greater than in the surrounding flow.

## Keywords

Boundary layer, compression corner, separation flow, shock wave, supersonic flow

Date received: 5 February 2018; accepted: 1 October 2018

## Introduction

One of the interesting specific features of supersonic separated flows is a possibility of the existence of extended local regions with gas-dynamic parameters (e.g. total pressure) that differ from the flow parameters in the surrounding flow.

One example of such regions is the region of interaction of shock waves of type IV in Edney's classification.<sup>1</sup> Interaction of the oblique and normal (bow) shock waves  $C_{01}$  and  $C_{02}$  (Figure 1(a)) leads to the formation of a triple configuration of shock waves  $C_1$ ,  $C_2$ ,  $C_T$ , and the so-called supersonic “jet”  $J$  in which the total pressure is higher than the total pressure in the subsonic flow surrounding the jet.

The separated flow where such interaction occurs may lead to the formation of a periodic self-sustained flow with pulsations in the frontal separation region (Figure 2(a)). This figure shows a sequence of frames composed of instantaneous (with the exposure time of  $\sim 1 \mu\text{s}$ ) schlieren pictures illustrating the time evolution of one cycle of pulsations.<sup>2</sup> Each photograph is put into correspondence to a normalized time instant (ranging from 0 to 1), which shows the phase of the process. This flow was first discovered by Mair,<sup>3</sup> and the analogy between type IV interaction and the axisymmetric shock wave structure formed in such a case was first noticed by Panaras.<sup>4</sup>

The pattern schematically presented in Figure 1(b) shows the interaction of shock waves in the flow around a blunted body with a spike, resulting in the formation of a high-total-pressure jet. The supersonic high-total-pressure annular jet formed due to interaction of the conical  $C_1$  and bow  $C_2$  shock waves is directed toward the head part of the model (see the pattern in Figure 2(b)). The reason for the formation of a periodic self-sustained flow is the pumping of the high-pressure gas by the jet into the separated reverse flow region  $RF$  (time instants 0.4–0.68 in the photographs in Figure 2(a)), followed by sudden emptying of the separation region due to its radial expansion after the instant when the jet moves away from the body surface (time instants 0.75–1.0); the self-oscillation mechanism is discussed further in Zapryagaev and Kavun.<sup>2</sup>

Another variant of interaction of shock waves with the formation of a high-total-pressure region of the flow near the wall is illustrated in Figure 3(a).

Khristianovich Institute of Theoretical and Applied Mechanics, Siberian Branch, Russian Academy of Sciences, Novosibirsk, Russia

## Corresponding author:

Valeriy I Zapryagaev, Khristianovich Institute of Theoretical and Applied Mechanics, Siberian Branch, Russian Academy of Sciences, Novosibirsk 630090, Russia.

Email: zapr@itam.nsc.ru

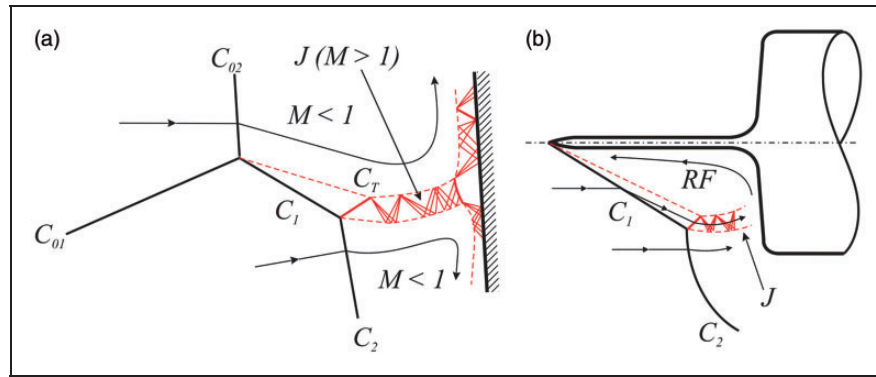


**Figure 1.** Interaction of shock waves with the formation of a jet impinging to the model surface: (a) type IV interaction (according to Edney<sup>1</sup>); (b) axisymmetric analog for a flow with a frontal separation region (according to Panaras<sup>4</sup>).

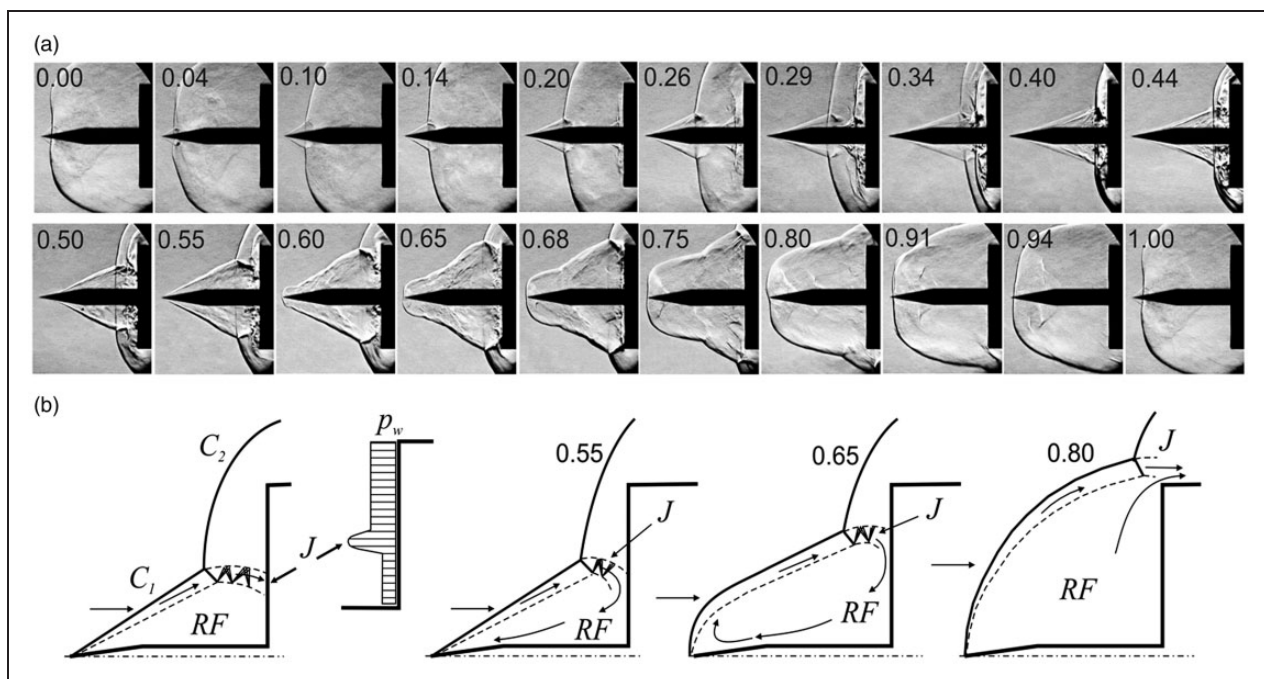


**Figure 2.** Self-sustained flow with the frontal separation region: (a) sequence of photographs of one cycle of pulsations (according to Zapryagaev and Kavun<sup>2</sup>); (b) flow pattern with the formation of a high-total-pressure jet  $J$  in the phase of the separation region formation and emptying (according to Panaras<sup>4</sup>).

This pattern was presented in Edney<sup>1</sup> on the basis of the data of Deveikis and Sawyer.<sup>5,6</sup> Interaction of the shock waves  $C_1$  and  $C_2$  leads to the formation of a jet  $J$  adjacent to the model surface. A known example of such a structure is a hypersonic flow around a double cone considered by Holden et al. (the pattern in Figure 3(b) is based on the data of Nompelis et al.<sup>7</sup>).

According to those results, interaction of the shock wave  $C_1$  attached to the first cone with the shock wave  $C_3$  detached from the second cone leads to the formation of a separation region with the separation shock wave  $C_2$ . The pattern also shows the reverse flow region  $RF$  and the slip surface  $SS$  passing downstream from the line of interaction of the shock waves  $C_1$  and  $C_2$ , which separates the gas flow that passed through the shock wave  $C_2$  from the flow that passed through

the shock wave  $C_2'$ . The shock waves  $C_2'$ ,  $C_3$ , and  $C_T$  form a triple configuration with an inhomogeneous flow region behind it: supersonic high-total-pressure jet  $J$  and region of the subsonic low-pressure gas behind the shock wave  $C_3$ . Between the model wall and the jet  $J$ , there is the boundary layer  $BL$ , where the total pressure is also lower than that in the jet.

It can be noted that the high-pressure region ("jet"  $J$ ) is formed in both cases owing to the flow passage through a system of oblique shock waves. The total pressure losses behind the oblique shock waves  $C_1$  and  $C_T$  are smaller than that behind the curved shock wave  $C_2$  (or  $C_3$ ), which is responsible for the difference in the total pressures in the jet  $J$  and in the flow surrounding the jet. The difference between the above-mentioned situations can be formulated as

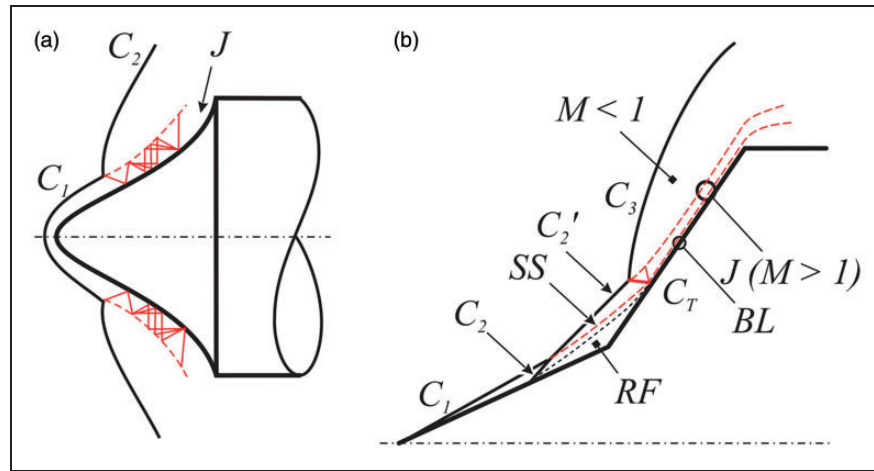


**Figure 3.** Interaction of shock waves with the formation of a jet adjacent to the model surface: (a) flow around a concave body (according to Edney<sup>1</sup> with a reference to Deveikis and Sawyer<sup>5,6</sup>); (b) flow around a double cone (according to Nompelis et al.<sup>7</sup>).

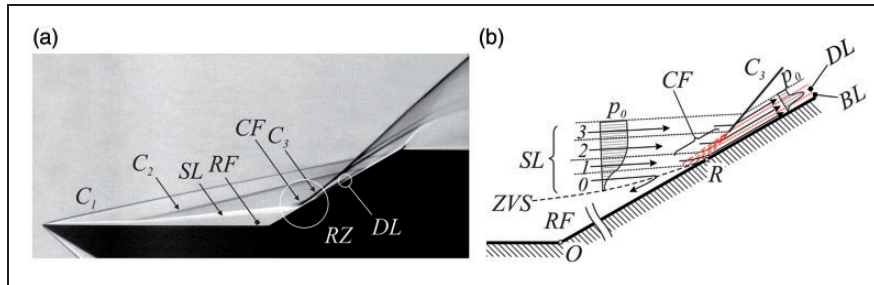


**Figure 4.** Supersonic separated flow in a compression corner: (a) schlieren picture; (b) diagram of the formation of the high-pressure layer DL (according to Zapryagaev et al.<sup>8,9</sup>).

follows: in the first case, the jet impinges onto the model surface in the close-to-normal direction with respect to the wall; in the second case, the jet moves along the model surface.

Another mechanism of the formation of the high-total-pressure gas region was proposed in Zapryagaev et al.<sup>8–10</sup> Based on the results of studying a separated flow in a compression corner, it was shown that the high-total-pressure gas region (called the “dynamic layer” by the authors) is formed due to passage of the incoming flow through an expansion fan formed in the flow reattachment region. According to the results obtained, the total pressure in the high-pressure region reached 0.95 of the free-stream total pressure.

A schlieren picture of this flow is shown in Figure 4(a), with an explanatory diagram in Figure 4(b). One can see the shock wave  $C_1$  from the leading edge of the compression corner, the separation shock  $C_2$ , the reattachment shock  $C_3$ , the reverse flow region  $RF$ , the shear layer  $SL$  above this region, the zero velocity surface  $ZVS$ , the reattachment zone  $RZ$ , the reattachment line  $R$  (which is normal to the plane of the figure and is shown as a point), the compression fan  $CF$ , the boundary layer  $BL$  downstream of the reattachment line, and the high total pressure “dynamic” layer  $DL$ .

The shear layer  $SL$  includes four conventional gas flows: 0–3 (Figure 4(b)). The gas flow indicated by 0 is directly adjacent to the zero velocity surface  $ZVS$ . The gas in this flow approaches the reattachment line  $R$ , but does not cross it; instead the gas enters the reverse flow region  $RF$ . The gas flows denoted by 1, 2, and 3 pass above the reattachment line  $R$  and are deflected parallel to the ramp wall. A compression fan  $CF$  is formed in the region ahead of the reattachment line  $R$ ; at a certain distance from the model wall, this compression fan transforms to the shock wave  $C_3$ . Flow 1, is characterized by a shear zone, becomes directly adjacent to the wall after having been deflected by  $CF$  and then feeds the boundary layer  $BL$ . Flow 2 is isentropically deflected in the compression fan  $CF$ . Flow 3 passes through the shock wave  $C_3$ . The losses of the total pressure  $p_0$  in layer 1 due to viscosity forces and in layer 3 on the shock wave  $C_3$  are greater than that in the compression fan  $CF$ , which leads to the formation of the high-total-pressure (“dynamic”) layer  $DL$  above the boundary layer  $BL$ .

Only one particular example of such a flow was considered in Zapryagaev et al.<sup>8–10</sup>: separated flow on a model with a ramp angle  $\varphi = 30^\circ$  for the free-stream Mach number  $M_\infty = 6$ . Therefore, it seems

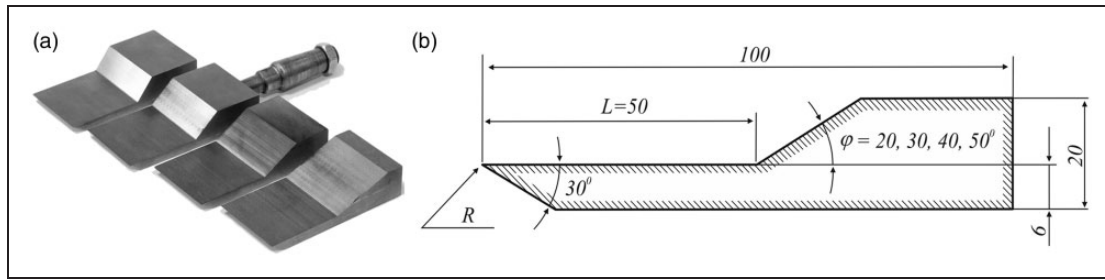


**Figure 5.** Model of the compression corner: (a) photograph of the models; (b) schematic of the model.

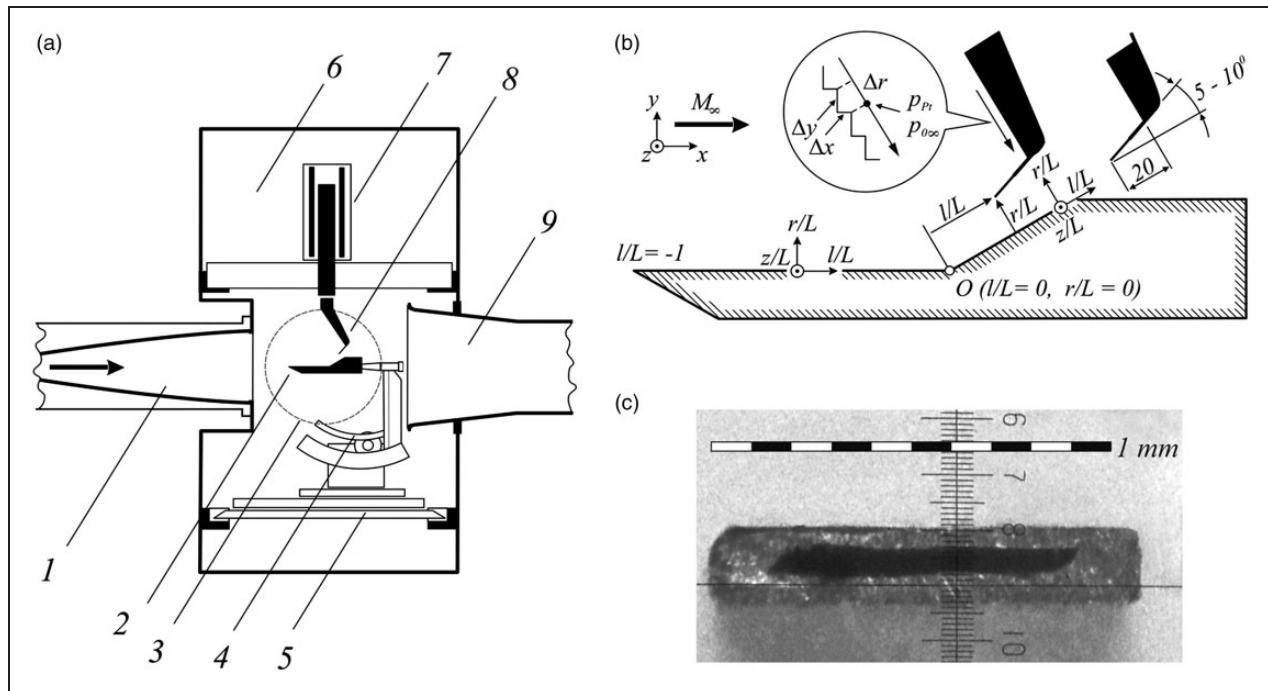


**Figure 6.** Arrangement of the experiment: (a) model mounted in the wind tunnel; (b) measurement of the Pitot pressure above the ramp surface; (c) tip of the Pitot probe.

reasonable to study the influence of the model geometry and free-stream Mach number on the characteristics and the region of existence of the high-pressure layer. In the present study, the flow downstream of the reattachment line is considered for the ramp angle varied in the interval  $\varphi = 20^\circ - 50^\circ$  in the flow with the Mach number  $M_\infty = 6$  and  $M_\infty = 8$ .

### Research technique

Four models (Figure 5(a)) of the compression corner were studied. All sizes of these models were identical except for the ramp angle, which was varied from  $20^\circ$  to  $50^\circ$ . The length of the horizontal flat plate was  $L = 50$  mm. The radius of curvature of the leading edge of the plate was  $R \sim 5\text{--}7\ \mu\text{m}$ . The model width was equal to the plate length  $L$ .

The experiments were conducted in the T-326 hypersonic blowdown wind tunnel based at ITAM SB RAS. The test section is the Eiffel chamber. The wind tunnel is

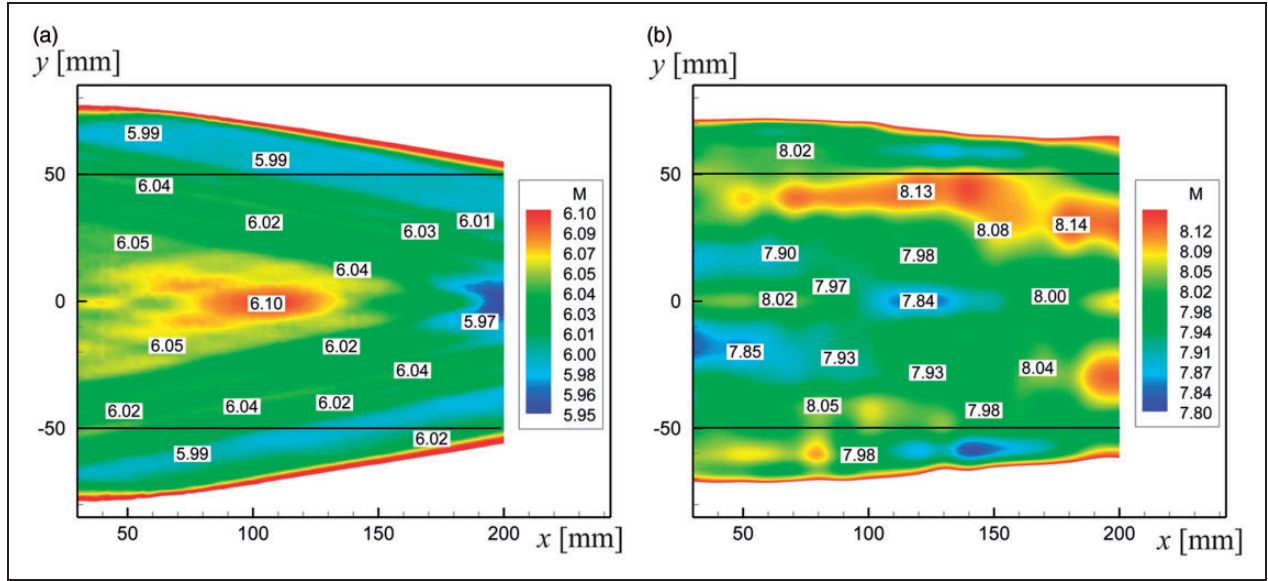
equipped with replaceable contoured axisymmetric nozzles with the exit diameter of 200 mm.

Figure 6 shows the arrangement of the experiment: model mounted in the test section (a); the coordinate system for Pitot pressure measurements (b) (the Pitot pressure is equal to the total pressure at the measurement point in a subsonic flow and to the total pressure behind the normal shock in a supersonic flow); and the shape of the tip of the Pitot pressure probe (c).

Figure 7 shows the Mach number field in the test section for  $M = 6$  (Figure 7(a)) and  $M = 8$  (Figure 7(b)). Local Mach number values were measured for different streamwise distances  $x$  using a Pitot tube. Mach number is calculated using the relation between freestream total pressure and Pitot pressure.

This wind tunnel ensures a homogeneous air flow at a distance  $x = 30\text{--}200$  mm from the nozzle exit, which is shaped as a cylinder 100 mm in diameter. The homogeneous flow regions are bounded by black horizontal lines:  $50 < y < +50$  mm. For  $M = 6$ ,





**Figure 7.** Mach number field in the test section of the T-326 wind tunnel: (a) in the nominal regime with  $M = 6$ ; (b) in the nominal regime with  $M = 8$ .

**Table 1.** Parameters of the experiment in the T-326 hypersonic wind tunnel.

Nominal operation mode of the wind tunnel	$M = 6$	$M = 8$
Pressure in the settling chamber, $p_0$ (Pa)	$9.68 \times 10^5$	$19.4 \times 10^5$
Temperature in the settling chamber, $T_0$ (K)	390–400	620–640
Mean Mach number in the homogeneous flow region, $M_m$	6.026	7.985
Reynolds number, $Re_L$	$6.1 \times 10^5$	$2.9 \times 10^5$
Measurement period (min)	5–15	

the mean Mach number in this region is  $M_m = 6.026$ , and the mean standard deviation is  $M_{Sd} = 0.016$  (0.2% of the mean value). For  $M = 8$ , the mean Mach number in this region is  $M_m = 7.985$ , and the mean standard deviation is  $M_{Sd} = 0.046$  (0.6% of the mean value).

The following elements are indicated by numbers in Figure 6(a): 1 – nozzle, 2 – model, 3 – window in the Eiffel chamber for observations, 4 – mechanism for changing the angle of attack of the model (in the present experiment,  $\alpha = 0^\circ$ ), 5 – device for model insertion into the flow, 6 – test chamber, 7 – three-axis traverse system designed for moving the measurement probes, 8 – pylon with the Pitot pressure probe, 9 – exhaust diffuser. The wind tunnel is started when the model is yet outside the flow. When a necessary flow regime is reached, the model is inserted into the flow by the device (5) within 1 s. This device is equipped with the alpha-mechanism, which allows the model to be aligned parallel to the incoming flow. The error of model mounting with respect to the free stream is about  $0.2^\circ$ . The model temperature before its insertion into the flow is  $\sim 295$  K.

The main parameters of the experiment are listed in Table 1. The experiment included schlieren

visualization of the flow around the model and Pitot pressure measurement above the ramp surface. The visualization was performed by the IAB-451 shadow-graph. The schlieren pictures were obtained with the horizontal position of the Foucault knife, and the exposure time was varied from 3 to 130  $\mu$ s for various runs. The photographs were taken by a Videoscanner-285/P-USB digital camera. The Pitot pressure was measured by a TDM-A-0.16 probe (the measurement range was  $0\text{--}1.6 \times 10^5$  Pa, and the probe error was smaller than 0.2% of the measurement range). The pressure probe data were recorded by an HP Agilent 34970A digital 14-bit multimeter. The pressure in the settling chamber of the wind tunnel was measured by a Metran-150-TAZ probe (the measurement range was  $0\text{--}25 \times 10^5$  Pa, and the measurement error was smaller than 0.1% of the measurement range). The measured pressure data were recorded by using an ADC module (IT-8). The maximum deviation from the nominal value (see Table 1) during the experiment was within 0.5%. The temperature in the settling chamber was measured by a chromel-alumel thermocouple, and the signal from the thermocouple was recorded by an ADAM 4018 ADC module. The error of temperature measurement in the

experiment was smaller than one degree. In the course of the experiment, the temperature in the settling chamber could change during the measurement period by 5–10 K.

The scheme of measurement of the Pitot pressure profile in the direction normal to the ramp plane is shown in Figure 6(b). The coordinate system  $(x, y, z)$  is referred to the free stream. The origin of the coordinate system is located at the point of intersection of the nozzle axis with the nozzle exit plane. In this coordinate system, commands are given for moving the pylon with the Pitot probe (device 7 in Figure 7(a)) by the traverse system; this device allows the probe to be installed with an error smaller than  $\pm 20 \mu\text{m}$  along each of the coordinate axes. The minimum step along each of the coordinates  $x, y, z$  is  $20 \mu\text{m}$ .

The coordinate system  $(l, r, z)$  is referred to the model. The origin of this coordinate system (point  $O$ ) is located in the plane of symmetry on the plane/ramp junction line. The coordinate line  $l$  is directed along the model surface, and the line  $r$  is normal to the wall. The coordinate  $z$  forms the right-hand coordinate system with the lines  $x, y$  and  $l, r$ . The Pitot pressure profiles measured in the coordinate system  $(x, y, z)$  are recalculated to the coordinate system  $(l, r, z)$ . The coordinate system  $(l, r, z)$  is normalized to the plate length  $L$ . The measurements were performed in the plane of symmetry of the model (plane  $z=0$ ) unless otherwise specified.

The pylon with the probe mounted on it is moved to a required cross section  $l/L$  at a height  $r/L$  above the wall surface. After that, the probe is moved toward the wall at prescribed steps  $\Delta x$  and  $\Delta y$  so that the following relation is satisfied:  $(\Delta x^2 + \Delta y^2)^{0.5} = \Delta r$ . The pressure was measured at the end of each displacement  $\Delta r$  after a delay necessary for pressure equalization in the measurement pipeline (1 s).

The length of the probe tube is 20 mm. The angle between the tube axis and the model surface (line  $O-l$ ) is  $5^\circ$ – $10^\circ$ , which is necessary to avoid insertion of disturbances generated by the pylon with the probe into the near-wall flow. The shape of the probe tip is shown in Figure 7(c). The height and width of the probe tip are 0.2 and 1.1 mm, respectively. The height and width of the probe orifice are 0.07 and 0.8 mm, respectively. It is assumed that the

probe measures the pressure in the geometric center of the pressure probe tip.

When the probe touches the wall, the electrical contact between the probe and model is closed, which is monitored by the probe motion control system. When the contact is closed, the control system issues a signal to terminate probe motion. In this position of the pylon with respect to the wall, it is assumed that the probe coordinate is equal to the half-height of the probe tip above the model surface  $r=0.1 \text{ mm}$ . After that, it is possible to calculate the distance  $r$  from the wall at which the pressure measurements were performed. This approach allows one to take into account the probe tip displacement with respect to the nominal coordinate  $(x, y, z)$  under the action of aerodynamic loads acting on the pylon with the probe. However, this measurement technique does not allow one to control possible premature closure of the electrical contact owing to vibrations of the probe tip under the action of flow pulsations in the near-wall region.

After the coordinate  $r/L$  is determined, the Pitot pressure profile  $p_{Pt}/p_{0\infty}(r/L)$  is constructed, where the experimentally measured pressure  $p_{Pt}$  is normalized to the total pressure measured at the same time in the settling chamber (which is assumed to be equal to the free-stream total pressure  $p_{0\infty}$ ).

Two series of experiments were performed, and 16 Pitot pressure profiles above the ramp wall were obtained (see Table 2, where the test series are indicated by Roman numbers I and II).

While analyzing the probe results it should be noted that the probe tip size is comparable to the characteristic size of the studied flow (the probe width is 2–4 times less than the distance from the model wall to the upper part of the  $DL$  layer).

Figure 8(a) shows the boundary layer structure in the absence of the probe. The distribution of Pitot pressure by boundary layer height in the  $x$  section is presented to the right of the plate in the same figure.

When the probe approaches the plate surface (Figure 8(b)) the near-wall flow structure may change. The shock wave  $C$  formed by the probe tip causes the three-dimensional separation zone  $Z$  to appear (on the model wall at centerline this zone is constrained by the separation point  $S$  and the

**Table 2.** Number and coordinates of the measured Pitot pressure profiles.

Ramp angle, $\varphi$ ( $^\circ$ )	20	30	40	50	30
Free-stream Mach number, $M_\infty$	6	6	6	6	8
Test series I					
Coordinate of the measurement cross section, $l/L$	0.46; 0.80	0.35	0.38; 0.46	–	0.40
Number of measured Pitot pressure profiles	2; 2	1	1; 1	–	2
Test series II					
Coordinate of the measurement cross section, $l/L$	0.46; 0.70	–	0.38	0.28; 0.32	–
Number of measured Pitot pressure profiles	1; 1 (+1 at $z/L=0.02$ )	–	2	1; 1	–

reattachment point  $R$ ). Near-wall streamline rise above the wall, increasing the boundary layer thickness  $\delta$ . Upstream from the separation line  $S$  the compression fan  $CF$  is formed, where the gas flow inside and above the boundary layer compresses isentropically with the increase of stagnation pressure and decrease of the Mach number. As a result, there is less total pressure loss behind the shock wave  $C$  and therefore the rise of the Pitot pressure measured with the probe (seen as a local maximum on the curve in the  $x$  section in Figure 8(b) to the right of the plate) in the upper region of the boundary layer. Due to its very small size, the separation zone  $Z$  is not usually visible on schlieren photographs.

To evaluate the influence the probe on the structure and gas-dynamic parameters distribution of the near-wall flow a special methodical study was conducted for  $M_\infty = 6$  on a sharp leading edge plate. The results showed that for small boundary layer thickness ( $\delta$  being 4 ... 5 times larger than the probe tip height) the probe influence becomes notable on the Pitot pressure curve (Figure 8(c), section  $x/L = 0.2$ ); however, in most cases this inaccuracy has no

influence on interpreting the experimental results for compression corner flows. There is an exception of one case, which is specifically discussed.

Experimental results are complemented with CFD data. The numerical computation was conducted using the ANSYS Fluent software. Compression corner flow with the geometry and dimensions of the  $20^\circ$  ramp angle model was studied.

The computation domain contained about 16 million cells. Near the model wall the grid was refined so that for the boundary layer thickness before the separation line there were about 50 grid cell layers. In a similar way, the grid was refined in the separated region and the reattachment zone of the flow for better resolution of the near-wall flow structure. During the computation Görtler-type streamwise vortex pairs were observed in the reattachment zone next to the ramp wall. The grid in this area was chosen so that for each streamwise vortex pair there were 50 grid layers in the vertical direction and 15–20 grid layers—in the transversal direction.

The leading edge of the model had a  $5\ \mu\text{m}$  blunting in the form of a vertical plane (approximately

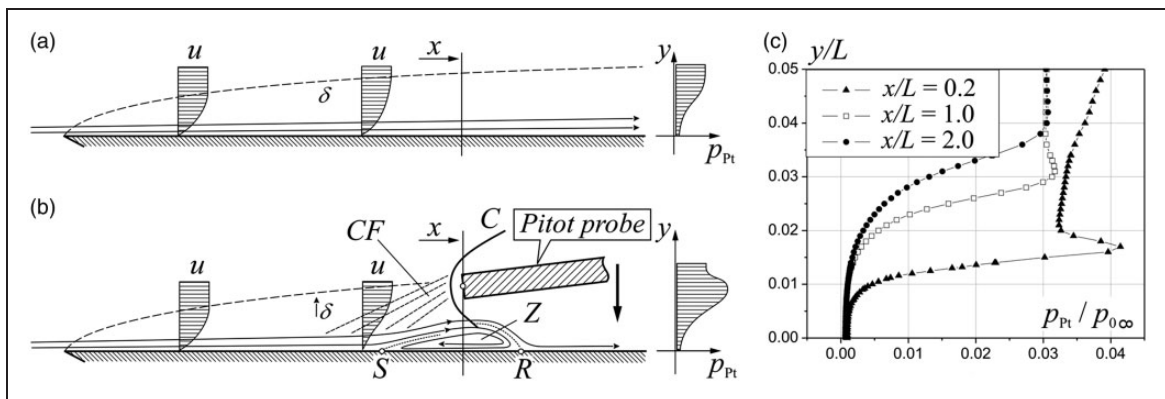


**Figure 8.** The probe influence on the near-wall flow structure: (a) boundary layer on the plate in the absence of the probe; (b) near-wall separated flow formed by the probe; (c) distributions of Pitot pressure by boundary layer height on the plate.

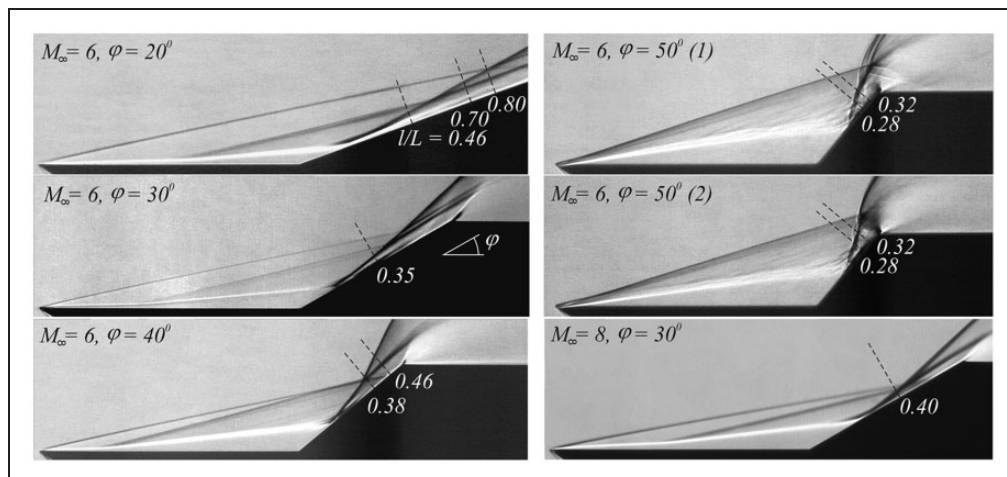


**Figure 9.** Schlieren pictures of a supersonic separated flow in a compression corner.

corresponding to the experimental model), there were 20 grid layers by edge height for the flow structure resolution near it.

All the computation parameters were chosen the same as the experimental conditions: free-stream Mach number  $M_\infty = 6.03$ , Reynolds number  $Re_L = 6 \times 10^5$ . At the computation domain input boundary the free-stream conditions were set:  $M_\infty = 6.03$ , static pressure 600 Pa, static temperature 47.5 K. At the output and side boundaries of the computation domain the reference conditions were set as follows: the static pressure of 600 Pa and the stagnation temperature of 393 K.

Three-dimensional laminar Navier–Stokes equations were solved. Second-order accurate Roe scheme was used. As the medium for the calculation viscous perfect gas was taken. Thermodynamic state of the gas was described by the Mendelev–Clapeyron equation. Gas thermal conductivity was assumed to be constant. The relation between thermal conduction coefficient and temperature was calculated using the Eucken formula. The heat flux between the model wall and the flow was absent, which corresponded to the adiabatic wall condition. The calculation results were used to analyze and interpret the experimental data.

## Results

The schlieren pictures of the flow above the compression corner surface are shown in Figure 9 (one photograph for each examined case except for the case with  $\varphi = 50^\circ$ , for which two photographs are presented: (1) and (2), which were taken at random time instants). The dashed lines show the cross sections where the Pitot pressure profiles were measured.

The shock wave structure of the flow in all pictures is similar to that in Figure 4(a). The flow structure includes the shock wave generated on the leading edge of the plate, the separation shock, the reattachment shock, the compression fan in the reattachment

region, the reverse flow region, and the shear layer above the latter. For the Mach number  $M_\infty = 6$ , an increase in the ramp angle  $\varphi$  makes the separation line shift upstream over the horizontal plate surface; in the case of  $\varphi = 50^\circ$ , the separation line closely approaches the leading edge. Moreover, in the case of  $\varphi = 50^\circ$ , disturbances in the shear layer  $SL$  can be seen above the reverse flow region, which reach the reattachment shock  $C_3$ ; for this reason, the reattachment shock has an inhomogeneous three-dimensional structure and oscillated in space with time.

To study the flow structure, we compared the schlieren pictures with the pressure measured by the probe. Figure 10(a) shows a schlieren photo of the flow in the reattachment zone for  $M_\infty = 6$ ,  $\varphi = 30^\circ$ ,  $l/L = 0.35$ . One can see the shock waves  $C_1$ ,  $C_2$ ,  $C_3$ , the compression fan  $CF$ , and the shear layer  $SL$  above the reverse flow region. The probe trajectory is indicated by the dashed line. Figure 10(b) shows the enlarged fragment of the photograph. For convenience of further comparisons, this fragment is rotated  $30^\circ$  clockwise so the ramp surface is horizontal. Points 1–6 indicate typical points of the flow on the Pitot pressure measurement line. In the photograph, the probe at first is in position 6 and then moves downward until it touches the model wall. The corresponding Pitot pressure profile is shown in Figure 10(c) (1 – experimental data, 2 – numerical data), where the vertical coordinate  $r/L$  has the same scale as in the photograph, which allows one to correlate the specific features of the pressure profile with the flow structure in the photograph.

The shock waves  $C_1$ ,  $C_2$ , and  $C_3$  are visible in the pressure profile as abrupt Pitot pressure changes (points 5, 4, and 3, respectively). In the region between the shock wave  $C_3$  and the model wall the probe registers a complex flow (indicated by the typical points 2 and 1). When the pictures were taken, the Foucault knife was oriented horizontally, thus making the vertical gradient of the gas density visible in the

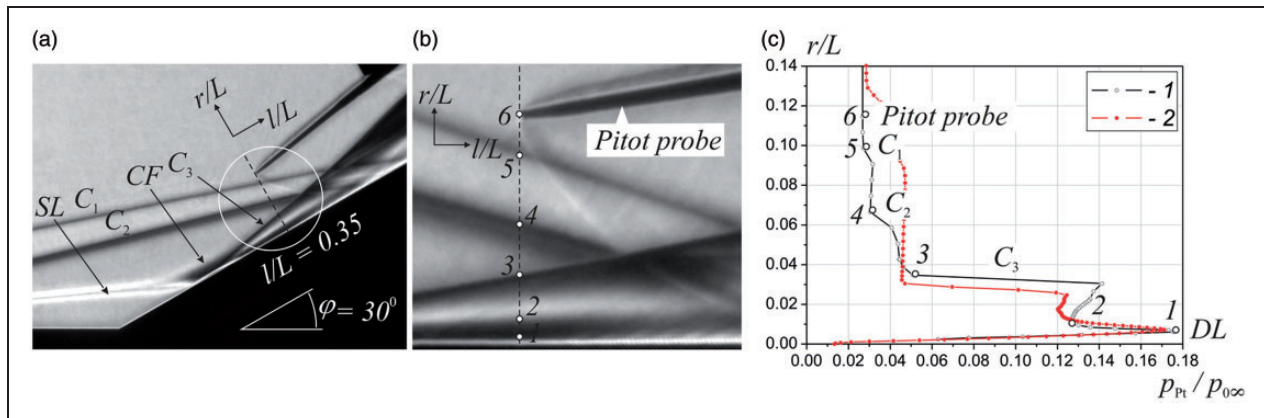


**Figure 10.** Correspondence between the shock wave structure and the Pitot probe measurements data,  $M_\infty = 6$ ,  $\varphi = 30^\circ$ , section  $l/L = 0.35$ : (a) schlieren photograph of the flow; (b) the same photograph (rotated  $30^\circ$  clockwise) enlarged in the probe measurement region; (c) Pitot pressure profile.



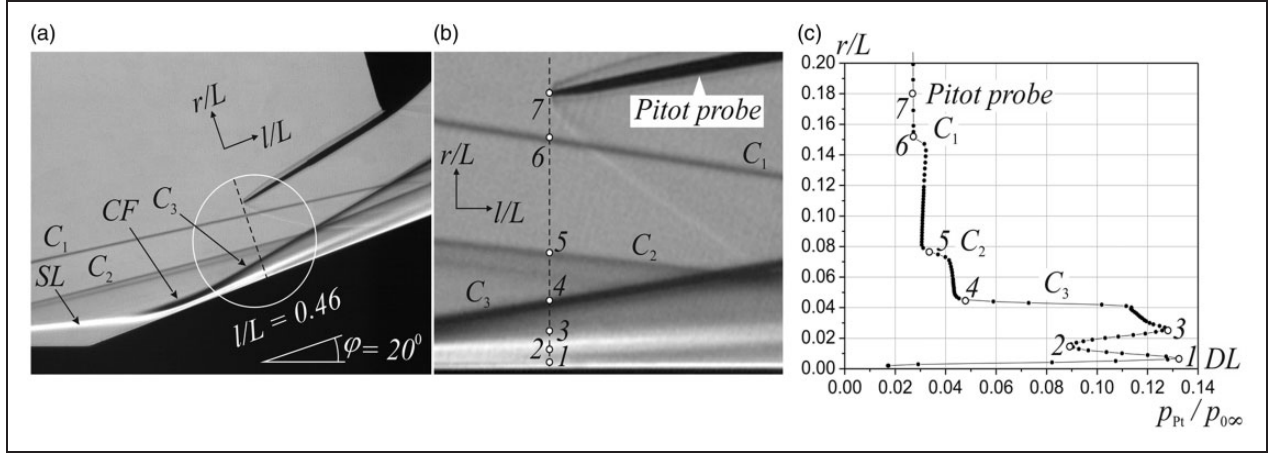


**Figure 11.** Correlation between the shock wave structure of the flow with Pitot pressure measurements for  $M_\infty = 6$ ,  $\varphi = 20^\circ$ , section  $l/L = 0.46$ : (a) schlieren picture of the flow; (b) magnified fragment of (a) in the region of probe measurements; (c) Pitot pressure profile.

photograph. Assuming the static pressure behind the  $C_3$  shock wave to be approximately uniform along the measurement line, the total pressure change in this direction (and, therefore, the Pitot pressure change) is caused by the dynamic pressure change. Further, the dynamic pressure is directly related to the gas density, therefore the nonuniformity of Pitot pressure vertical distribution is related to the nonuniformity of density distribution, which should be visible from the photograph.

Moreover, it should be noted that a beam of light passes through the entire flow field, including all the density irregularities on the way, so the picture seen in the photograph is actually a plane projection of the spatial structure of the flow. For example, the shock waves  $C_1$ ,  $C_2$ ,  $C_3$  are curved in the direction orthogonal to the photograph plane and are therefore seen as stripes of finite width and not thin lines. The shock wave  $C_2$  has the largest curvature and thus appears to be the widest.

In the schlieren photograph (Figure 10(b)) when moving downward the density increase is depicted as darker regions and the density decrease—as lighter regions. Then, above point 2 the density decreases (the light region), and below it increases (the dark region). A similar dependency of the Pitot pressure change can be seen on the profile in Figure 10(c) (curve 1). Below point 1 the density starts to decrease again (a very thin light area can be seen near the ramp surface), which also corresponds to the probe data (the Pitot pressure is reduced near the wall). Therefore, the visualization data and the probe measurements are in qualitative accordance.

As a result the Pitot pressure profile has a local maximum near the wall, labeled as  $DL$  in Figure 10(c) (high-total-pressure or dynamic layer). This maximum shows the existence of high dynamic pressure gas layer near the wall, which signifies that the total pressure in this layer is higher than in surrounding gas layers as well. Comparing the peak

amplitude ( $p_{Pt}/p_{0\infty} \sim 0.18$ ) to the results of methodical experiment in Figure 8(c), one can conclude that the probe error of the Pitot pressure measurement is insignificant for analyzing the final results. Besides, similar structure of the near-wall flow can be found in calculation, and the distance between the high-total-pressure layer  $DL$  and the ramp surface and its amplitude correspond well in experimental and numerical data (curves 1 and 2 in Figure 10(c), confirming the probe measurements validity and the accuracy of schlieren photograph interpretation.

A more complicated flow pattern for the  $M_\infty = 6$ ,  $\varphi = 20^\circ$ , and  $l/L = 0.46$  is shown in Figure 11. Figure 11(a) shows the schlieren picture of the flow in the region of flow reattachment; one can see the shock waves  $C_1$ ,  $C_2$ ,  $C_3$ , the compression fan  $CF$ , and the shear layer  $SL$  above the reverse flow region. The probe trajectory is indicated by the dashed line. Figure 11(b) shows the enlarged fragment of the photograph in Figure 10(a). For convenience of further comparisons, this fragment is rotated  $20^\circ$  clockwise so that the ramp surface is horizontal. Typical points of the flow on the Pitot pressure measurement line are indicated by numbers 1–7. In the photograph, the probe is in position 7 and then moves downward until it touches the model wall. The corresponding Pitot pressure profile is shown in Figure 11(c).

The shock waves  $C_1$ ,  $C_2$ , and  $C_3$  are visible in the pressure profile as abrupt Pitot pressure changes (points 6, 5, and 4, respectively). After the reattachment shock  $C_3$ , the density first increases from point 4 to point 3 (dark region), then decreases (points 3–2), increases one more time (points 2–1), and again decreases near the wall. The same dependence of the Pitot pressure can be seen in Figure 11(c). Therefore, this complicated dependence of the experimentally measured Pitot pressure distribution is confirmed by optical visualization of the flow in the near-wall region.

Hence, the probe measurement accuracy is confirmed by qualitative correspondence to the schlieren

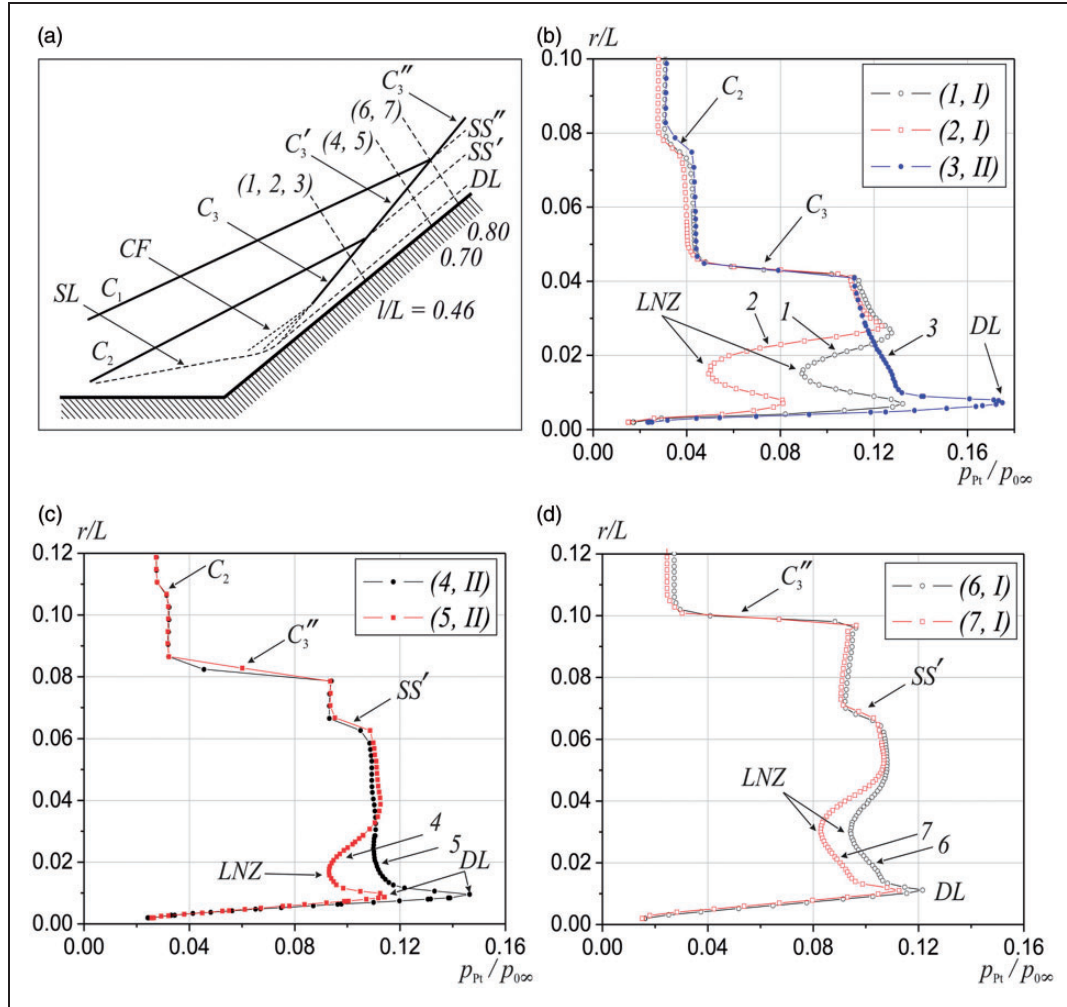


**Figure 12.** Flow structure and Pitot pressure distribution near the ramp wall for the case with  $M_\infty = 6$  and  $\varphi = 20^\circ$ : (a) simplified pattern of the separated flow in the compression corner; (b) Pitot pressure profiles in the cross section  $r/L = 0.47$  (curves 1–3); (c) Pitot pressure profiles in the cross section  $r/L = 0.70$  (curves 4 and 5); (d) Pitot pressure profiles in the cross section  $r/L = 0.80$  (curves 6 and 7).

photograph, which allows the Pitot pressure distribution to be analyzed. The profiles of the measured Pitot pressure are shown in Figures 12 and 13. Figure 12(a) shows a simplified pattern of the shock wave structure of the flow for  $\varphi = 20^\circ$ , which includes some elements of the separated flow in the compression corner in the plane of symmetry of the flow. The slip surfaces  $SS'$  and  $SS''$  separate the gas flows with various total pressures, which passed through the shock waves  $C_3$ ,  $C_3'$ , and  $C_3''$ . The test series are indicated by I and II. In both experimental series the flow was probed at the model symmetry axis at  $z = 0$ . Figure 12(b) to (d) presents the Pitot pressure distributions at various distances from the beginning of the ramp for the  $\varphi = 20^\circ$  model. Figure 13 shows the Pitot pressure distributions for the  $\varphi = 30^\circ$  model and Mach numbers  $M_\infty = 6$  (Figure 13(a)) and  $M_\infty = 8$  (Figure 13(b)), as well as the  $\varphi = 40^\circ$  and  $\varphi = 50^\circ$  models (Figure 13(c) and (d)).

The coordinate  $r/L = 0$  corresponds to the model wall, and  $r/L = 0.002$  is the half-height of the probe tip in the position where it touches the model wall.

For  $M_\infty = 6$  and  $\varphi = 50^\circ$ , the lowest position of the probe  $r/L = 0$  can be obtained with a small error ( $r/L \sim 0.002$ ) because of premature closure of the electrical contact due to probe tip vibrations under the action of flow pulsations in the near-wall region of the flow.

A local peak of the Pitot pressure (dynamic layer  $DL$ ) is seen in all graphs near the wall at the height  $r/L = 0.005$ – $0.01$ . Therefore the experimental data suggests that the dynamic layer exists for all studied models. Good agreement of the results in the upper part of the Pitot pressure profiles (positions and intensities of the shock waves and slip surfaces) can be noted for various experiments and even various test series (see Figure 13(c), lines 11 and 13). In the lower part, however, the experimental data diverge. Thus, the flow structure is similar in the upper part of the flow, but differs from experiment to experiment near the model wall. The most noticeable differences are observed in the case with  $M_\infty = 6$  and  $\varphi = 20^\circ$ . In Figure 12(b) to (d), one can see regions of reduced Pitot pressure denoted by  $LNZ$  (local nonuniformity zones). A notable divergence is also present for the

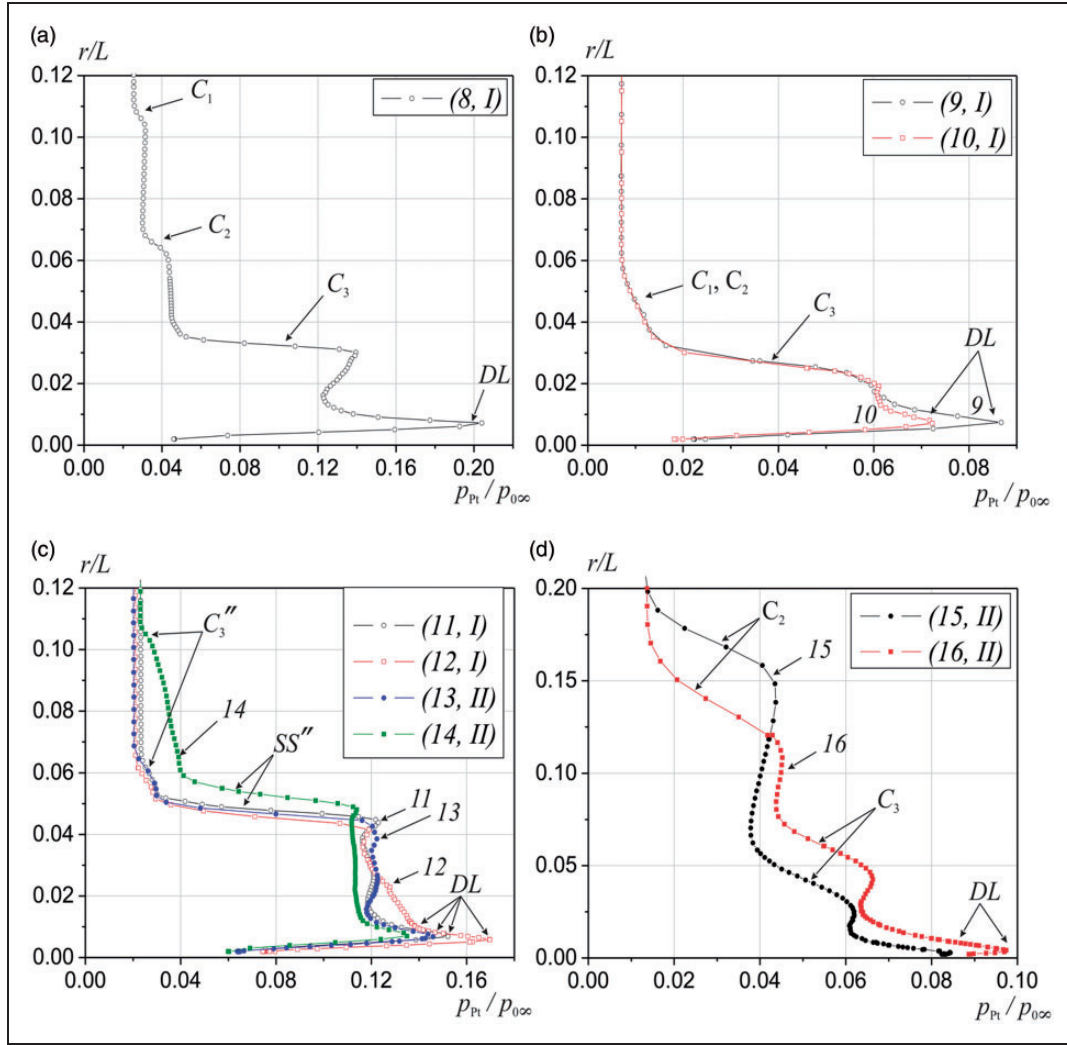


**Figure 13.** Pitot pressure distribution near the ramp wall: (a)  $M_\infty = 6, \varphi = 30^\circ$ , cross section  $r/L = 0.35$  (curve 8); (b)  $M_\infty = 8, \varphi = 30^\circ$ , cross section  $r/L = 0.40$  (curves 9 and 10); (c)  $M_\infty = 6, \varphi = 40^\circ$ , cross sections  $r/L = 0.38$  (curves 11, 12, and 13) and  $r/L = 0.46$  (curve 14); (d)  $M_\infty = 6, \varphi = 50^\circ$ , cross sections  $r/L = 0.28$  (curve 15) and  $r/L = 0.32$  (curve 16).

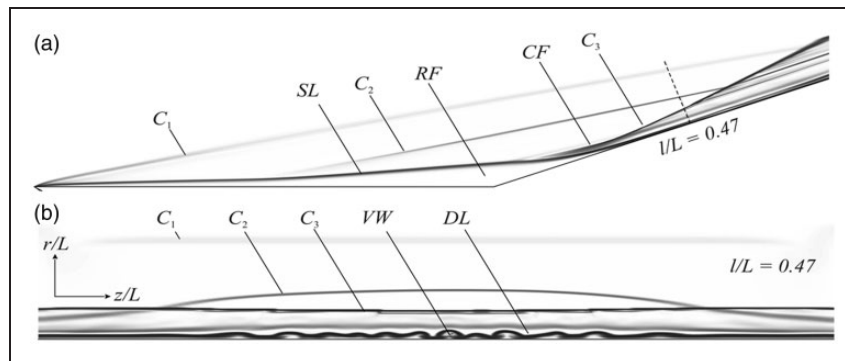


**Figure 14.** Calculated flow pattern for the compression corner  $M_\infty = 6, \varphi = 20^\circ$ : (a) center plane flow structure ( $z = 0$ ); (b) flow structure in section  $l/L = 0.47$ .

cases of  $M_\infty = 6, \varphi = 40^\circ$  (Figure 13(c)) and  $M_\infty = 8, \varphi = 30^\circ$  (Figure 13(b)).

To clarify the near-wall flow structure observed in Figure 11 and recorded in Figures 12 and 13, an

additional numerical simulation was conducted. Figure 14 shows the calculated flow structure in the  $z = 0$  plane (Figure 14(a)) and in the section  $l/L = 0.47$  (Figure 14(b)). All the main elements of

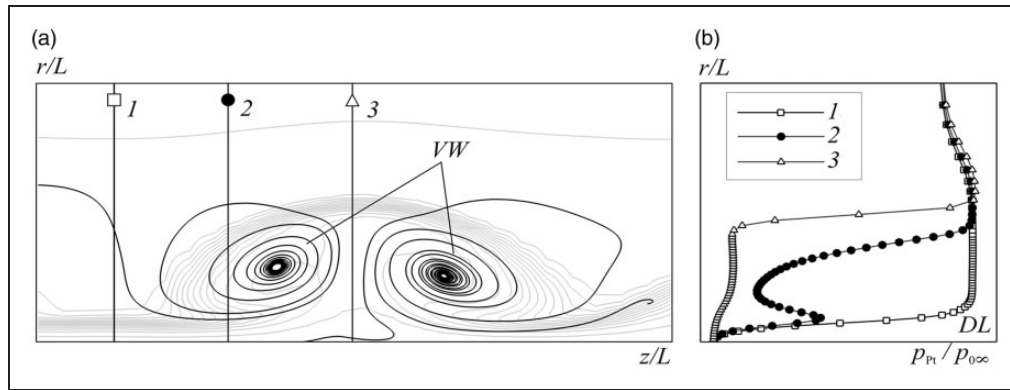


**Figure 15.** Calculated vortex flow structure near the ramp wall, constructed from the Pitot pressure distribution for the case  $M_\infty = 6$ ,  $\varphi = 20^\circ$ , section  $l/L = 0.47$ : (a) streamwise near-wall vortex pair; (b) characteristic Pitot pressure profiles in the same section for various  $z/L$  coordinate values.

the separated flow described earlier can be noted: the leading edge shock wave  $C_1$ , the separation shock wave  $C_2$ , the reattachment shock wave  $C_3$ , the reverse flow region  $RF$ , the shear layer  $SL$ , the compression wave fan  $CF$ , and the high-total-pressure layer  $DL$ . Furthermore, in the cross-section  $l/L = 0.47$  (Figure 14(b)) one can see a system of wall-adjacent vortices  $VW$ . The last two elements of the flow structure ( $DL$  and  $VW$ ) in the reattachment zone are enlarged in Figure 15. Figure 15(a) shows the streamwise vortex pair  $VW$  located near the wall, and Figure 15(b) shows the corresponding Pitot pressure distribution along three reference coordinate lines: between the neighboring vortices (curve 1), on the edge of the vortex pair region (curve 2), in the middle of the vortex pair region (curve 3).

Wall-adjacent streamwise vortex pairs also appear in the computation for the  $M_\infty = 6$ ,  $\varphi = 30^\circ$  case. For the supersonic separated flow these vortices were first observed in experiments and described in Ginoux.<sup>11</sup> Their formation mechanism is associated with the instability of the shear layer  $SL$  under the action of centrifugal forces in the reattachment zone (Görtler-type shear flow instability), which is also confirmed by the results in Zapryagaev and Kavun.<sup>10</sup>

When compared, experimental and numerical Pitot pressure distributions are in qualitative agreement (experimental curves 1 and 2 in Figure 12(b) and numerical curve 2 in Figure 15(b)). Based on this it can be assumed that the complex pattern of the near-wall flow, seen on the schlieren photograph (Figure 11(b)) is connected to the formation of a streamwise vortex pairs system near the ramp wall, and the local pressure peaks below the  $LNZ$  regions recorded on the corresponding Pitot pressure profiles (Figure 12(b) to (d)) stem from the vortices  $VW$  entraining high-total-pressure gas from the  $DL$  layer to the near-wall region.

On the other hand, the Pitot pressure maximum  $DL$  on curve 3 (Figure 15(b)) is relatively small compared to pressure behind the  $C_3$  shock wave, and at

the calculation results there are no profiles similar to curve 3 in Figure 12(b), which presents in the experiment. This fact makes it impossible to claim the experimental data obtained by probe measurements to be accurate for this compression corner geometry. Nevertheless, the calculated pressure maximum is present in Figure 15(b), which confirms the existence of the high-total-pressure layer  $DL$  in this case as well, and its small relative size is caused by low total pressure loss on the weak reattachment shock  $C_3$ , which inclined at a low angle to the ramp surface.

## Conclusions

The present experimental investigation showed that the high-total-pressure layer (dynamic layer  $DL$ ) is formed in the reattachment zone of a hypersonic separated flow in the range of the ramp angles from  $20^\circ$  to  $50^\circ$  for Mach number 6. The high-total-pressure layer is also detected for Mach number 8 and  $30^\circ$  compression corner angle.

The physical mechanism of high-pressure layer formation is associated with the presence of a compression wave fan located near the reattachment zone, where this part of the flow undergoes an isentropic compression with little total pressure loss, which leads to high total pressure value in this layer.

With the ramp angle increase (up to  $50^\circ$ ) the flow structure changes—the separation line moves to the plate leading edge and the reattachment line moves to the ramp top. In this case intensive flow pulsations are observed.

The high-total-pressure layer formation is followed by the development of streamwise vortices related to the Görtler-type shear flow instability in the reattachment zone, which influences the spatial structure and gas-dynamic parameters of the near-wall flow.

The presence of the high-total-pressure layer for a wide range of ramp angles and different Mach



numbers suggests that it may exist in other flows with reattachment of supersonic separated flow.

### Declaration of Conflicting Interests

The author(s) declared no potential conflicts of interest with respect to the research, authorship, and/or publication of this article.

### Funding

The author(s) disclosed receipt of the following financial support for the research, authorship, and/or publication of this article: this research was carried out within the framework of the Program of Fundamental Scientific Research of the state academies of sciences for 2013-2020 (project AAAA-A17-117030610137-0).

### ORCID iD

Valeriy I Zapryagaev  <http://orcid.org/0000-0002-6331-1960>

### References

1. Edney B. Anomalous heat transfer and pressure distribution on blunt bodies at hypersonic speeds in the presence of an impinging shock. Aeronautical Research Institute of Sweden, 1968, Report 115, 93 pp.
2. Zapryagaev VI and Kavun IN. Experimental study of the reverse flow in the forward separation region in a pulsating flow around a spiked body. *J Appl Mech Techn Phys* 2007; 48: 492–500.
3. Mair W. Experiments on separated boundary layers on probes in front of blunt nosed bodies in a supersonic air stream. *Philos Mag* 1952; 43: 695–716.
4. Panaras AG. Pulsating flows about axisymmetric concave bodies. *AIAA J* 1981; 19: 804–806.
5. Deveikis WD and Sawyer JW. Aerodynamic characteristics of tension shell shapes at Mach 3.0. NASA TN D-3633, 1966, 51 pp.
6. Sawyer JW and Deveikis WD. Effects of configuration modifications on aerodynamic characteristics of tension shell shapes at Mach 3.0. NASA TN D-4080, 1967, 38 pp.
7. Nompelis I, Candler GV and Holden MS. Effect of vibrational non-equilibrium on hypersonic double-cone experiments. *AIAA J* 2003; 41: 2162–2169.
8. Zapryagaev VI, Kavun IN and Lipatov II. Supersonic laminar separated flow structure at ramp for free-stream Mach number 6. In: Reijasse Ph, Knight D, Ivanov M and Lipatov I (eds) *Progress in flight physics*. EUCASS advances in aerospace sciences book series. France: EDP Sciences, Torus Press, 2013, pp.349–362.
9. Zapryagaev VI, Kavun IN and Lipatov II. High-pressure layer generation in a compression corner at a supersonic flow velocity. *Fluid Dyn* 2014; 49: 819–826.
10. Zapryagaev VI and Kavun IN. Formation of streamwise vortices behind the line of supersonic separated flow reattachment at a compression corner. *TsAGI Sci J* 2016; 47: 267–281.
11. Ginoux JJ. Streamwise vortices in reattaching high-speed flows: a suggested approach. *AIAA J* 1971; 9: 759–760.

## Appendix

### Notation

$l$	streamwise coordinate (directed downstream along the model)
$L$	length of the horizontal flat plate
$M$	Mach number
$M_m$	mean Mach number in the considered domain
$M_{Sd}$	standard deviation of the Mach number from the mean value $M_m$
$M_\infty$	free-stream Mach number
$p$	pressure
$p_0$	total pressure
$p_{0\infty}$	free-stream total pressure
$p_{Pt}$	Pitot pressure measured by the probe
$p_w$	near-wall pressure (pressure on the model surface)
$r$	normal coordinate (perpendicular to the model surface)
$R$	radius of curvature of the leading edge of the flat plate
$Re$	Reynolds number
$Re_L$	Reynolds number based on the plate length $L$
$T$	temperature
$T_0$	total temperature
$T_{0\infty}$	free-stream total temperature
$x$	horizontal coordinate in the free-stream direction
$y$	vertical coordinate
$z$	transverse coordinate (forming together with the coordinates ( $l$ and $r$ ) and ( $x$ and $y$ ) the right-hand coordinate system ( $l, r, z$ ) and ( $x, y, z$ ))
$\alpha$	angle of attack of the model
$\varphi$	ramp angle